**Chem, Volume 7**

## Supplemental information

# Observation of a potential-dependent switch of water-oxidation mechanism on Co-oxide-based catalysts

**Chaochao Lang, Jingyi Li, Ke R. Yang, Yuanxing Wang, Da He, James E. Thorne, Seth Croslow, Qi Dong, Yanyan Zhao, Gabriela Prostko, Gary W. Brudvig, Victor S. Batista, Matthias M. Waegele, and Dunwei Wang**

# Supporting information

## EXPERIMENTAL PROCEDURES

### *Materials*

$Co(NO_3)_2$ (99.999%, Alfa Aesar), KOH (85%, VWR International), $NaNO_3$ (99.0% min., Alfa Aesar), $NaClO_4$ (99.0% min., Alfa Aesar), $KNO_3$ (99.0% min., Sigma-Aldrich), $K_2HPO_4$ (98.0% min., Alf Aesar), $KH_2PO_4$ (98.0% min., Alf Aesar), $Na_2HPO_4$ (99.0% min., Fisher chemical) and $C_2H_3NaO_2$ (99.0% min., Sigma-Aldrich) were used as received. HF (48 wt.%), $NaAuCl_4 \cdot 2H_2O$ (99.99%; metals basis), $Na_2SO_3$ (98.5%; for analysis, anhydrous), $Na_2S_2O_3 \cdot 2H_2O$ (99.999%; trace metal basis), $NH_4Cl$ (99.999%; metal basis), and $KNO_3$ (99.999%, trace metal basis) were used as received from Fisher Scientific. All electrolyte solutions were prepared with deionized water (Barnstead, 18 MΩ-cm resistivity). $H_2{}^{18}O$ (97% enriched) was used as received from Medical Isotopes, NH. $D_2O$ (99.9%) was used as received from Aldrich.

### *Au Nanofilm Preparation*

The gold nanofilm was electrolessly deposited onto Si wafers (IRUBIS GmbH, Germany) following the reported method.[1] The reflective surface of the Si wafer was polished on a mat using 6 and 1 µm diamond slurries (Ted Pella; Redding, CA), then 0.05 µm alumina paste (Electron Microscopy Sciences; Hatfield, PA) with cotton swabs, for 5 min respectively. Then, the Si wafer was cleaned with five consecutive 5 min sonication in ultrapure water and acetone alternately. For the deposition, the Si wafer was first etched in 40% $NH_4F$ for 90 s to remove surface oxide and terminate the surface with hydrogen atoms. Au nanofilm was plated by immersing the Si wafer into a 2:1 mixture of a plating solution and 2% HF at 60 °C for 120 s. The plating solution contains 15 mM $NaAuCl_4 \cdot 2H_2O$, 150 mM $Na_2SO_3$, 50 mM $Na_2S_2O_3 \cdot 2H_2O$, and 50 mM $NH_4Cl$. The resulted resistance of the gold film is 5-10 Ω.

### *Co-Pi or $CoO_x(OH)_y$ Film Deposition*

Co-Pi catalysts were electrodeposited onto substrates in a solution of 0.5 mM $Co(NO_3)_2$ and 0.1 M phosphate buffer (KPi) (pH=7.0) using a Solartron analytical potentiostat by potentiastatical deposition at a potential of 1.14 V vs. the normal hydrogen electrode (NHE) with the passage of 20 mC $cm^{-2}$.[2] $CoO_x(OH)_y$ electrodes were electrodeposited onto the Pt substrates or Au films in a solution of 10 mM $Co(NO_3)_2$ and 0.1 M $NaCH_3CO_2$ using a VersaStat3 potentiostat (AMETEK; Berwyn, PA). The galvanostatical deposition was set at an anodic current density of 0.05 mA $cm^{-2}$ vs. Pt counter electrode for 5 min.[3]

### *General Electrochemical Methods*

All electrochemical experiments were conducted using a CH Instruments or Solartron analytical potentiostat, a Ag/AgCl reference electrode (0.197 V) or a saturated calomel electrode (SCE, 0.242 V), and a Pt counter electrode. Two types of substrates were used for working electrodes: fluorine-doped tin oxide (FTO) electrode and Pt rotating disk electrode. All the electrochemical measurements were conducted on Co-Pi-coated FTO electrodes in a single cell unless otherwise stated. Rotating disk electrode measurements were conducted using a Pine Instruments MSR rotator and a 5 mm diameter Pt-disk rotating electrode. All electrochemical experiments were performed using a three-electrode electrochemical cell containing a ~15 mL electrolyte solution. Unless otherwise stated, all experiments were performed at ambient

temperature and electrode potentials were converted to the reversible hydrogen electrode (RHE) scale using an equation: $E(\text{RHE}) = E(\text{RE}) + E^{o}(\text{RE}) + 0.059 \times \text{pH}$, $E$(RHE) and $E$(RE) are the potential versus RHE and reference electrode, $E^{o}$(RE) is the potential of reference electrode. The electrolyte resistance between working electrode (WE) and RE was measured by electrochemical impedance spectroscopy (EIS) and the resistance was used for $iR$ compensation. $E(\text{RE})_{\text{actual}} = E(\text{RE})_{\text{measured}} - iR$ ($i$ and $R$ are the values of current and solution resistance, respectively).

All the water-in-salt (WiS) electrolyte solutions used in the experiments were freshly prepared before every single test. To make the water-in-salt solutions, we first prepared KPi buffer solutions and then added salts into the KPi buffer solutions. pH of all the solutions was adjusted to 7.0 with a freshly prepared 6 M KOH solution in order to prevent the influence of pH on water oxidation activity. Based on the previous literature,[4] water activities ($a_w$) in 0 m $NaNO_3$ @ 0.1 M KPi , 2 m $NaNO_3$ @ 0.1 M KPi, 4 m $NaNO_3$ @ 0.1 M KPi, 7 m $NaNO_3$ @ 0.1 M KPi are calculated as 1, 0.94, 0.89, 0.83, respectively.

### *Details of the Electrochemical Measurements*

The data in Figures 3a and 3b were collected under steady-state condition, each set of data were repeated three times with a freshly prepared catalyst of similar activity. During the data collection process, the steady-state measurement was performed for about 5 minutes until the current was stable, and then the data was processed by making an average of the last 20 raw data points in steady-state current density vs. potential ($j$-$E$) plots (Figure S6 is a representative example of data collection). The data in Figures S7 and S9-S16 were collected under steady-state condition for 3 to 5 min depending on the experiment. The data was processed by making an average of the last 20 raw data points. For Figures S17 and S20, the samples were subjected to 3 consecutive CV measurements. The second and third CV cycles show consistent result, so the third CV cycles were shown. For Figure S19: The data were collected with the same catalyst; we first measured the cyclic voltammetry (CV) plot in $D_2O$ at a scan rate of 20 mV $s^{-1}$ and then performed the same measurement in $H_2O$.

### *SEIRAS-ATR Measurement*

All in-situ surface-enhanced infrared absorption spectroscopy in attenuated total reflection mode (SEIRAS-ATR) measurements were carried out using nitrogen-purged Bruker Vertex 70 FTIR spectrometer (Billerica, MA) equipped with a liquid-nitrogen-cooled MCT detector (FTIR-16; Infrared Associates; Stuart, FL). The catalyst coated Si wafer was assembled into a customized polyether ether ketone (PEEK) spectroelectrochemical cell, and coupled vertically with an ATR accessory (VeeMax III; Pike Technologies; Madison, WI). All experiments were run with an incident angle of 50°, a resolution of 4 $cm^{-1}$, and a scanner velocity of 40 kHz. For all spectra shown, change in optical density was calculated according to Absorbance = -log($S$/$R$), with $S$ and $R$ referring to the single beam sample spectrum and single beam reference spectrum, respectively.

Before and after spectroscopic measurements, the quality of the film electrodes was confirmed by carrying out a CV from 1.0 to 1.6 V vs. Ag/AgCl (1.61 to 2.21 V vs. RHE) at a scan rate of 20 mV $s^{-1}$. All presented spectra were collected with electrodes that exhibited Co(II)/Co(III) redox peaks in the CVs and a water oxidation current (Figure S2).

For spectroscopic measurements, the $CoO_x(OH)_y$ electrode potential was stepped in 0.1 V increments from 2.21 to 1.61 V vs. RHE. The steps were connected by potential ramps of 20 mV $s^{-1}$. Each potential was held for 120 s. During this time, infrared spectra were collected. Spectra collected at 2.21 and 2.01 V (sample potentials) are shown in Figures 2 and S3-S5. The single beam spectra collected at 1.61 V vs. RHE served as the reference spectrum. A leakless Ag/AgCl (ET072-1; eDAQ, Colorado Springs, CO) and Pt wire (99.95%; BASi Inc.; West Lafayette, IN) were used as reference electrode and counter electrode, respectively. The electrolyte was prepared with 0.1 M KPi in $D_2O$, $H_2O$, or $H_2{}^{18}O$ at pH = 7, and the solution pD value was corrected with a factor of 0.4 from the reading of a pH meter.[5]

### *Faraday Efficiency Measurement*

Faradaic efficiency (FE) was measured with gas chromatography-online method (GCMS-QP2010, Shimadzu). A piece of FTO (1×3 $cm^2$) was used for growing Co-Pi catalyst. The method for growing the catalyst is the same as that described in the Co-Pi or $CoO_x(OH)_y$ Film Deposition part. $O_2$ gas was detected. During the experiment, the Co-Pi-coated FTO electrode was immersed into a reaction cell containing about 20 mL 0.1 M KPi neutral electrolyte. A constant current (3 mA) was applied to the electrode in order to generate $O_2$ bubbles. Then, the $O_2$ gas was further purged into the gas line of gas chromatography–mass spectrometry (GC-MS) for FE measurement. The equation for calculating FE is given below:

$$FE = \frac{4 \times Oxygen\ amount\ (umol \cdot\ s^{-1})}{Charge\ (umol \cdot\ s^{-1})} \times 100\%$$

### *Computational Details*

All DFT calculations were performed with Gaussian 16 Revision C01 software package.[6] We used the B3LYP functional[7,8] in conjugation with the def2-SV(P) basis set[9] for all atoms in the geometry optimization. Frequency analysis was performed to verify the nature of obtained stationary points and obtain harmonic frequencies to calculate the zero-point energies and thermal correction to the entropy and free energy. We used the def2-TZVP basis set[9] for single-point energy calculation to final composite free energy changes. The solvation effect was considered the SMD implicit solvation model[10] and the dispersion correction was considered using Grimme's empirical dispersion correction version 3 with Becke-Johnson damping.[11] We performed geometry optimization in both gas phase and dielectric continuum with SMD. We found that the geometry relaxation in the solvation is quite significant (Figure S22); therefore, all the geometries except $H_2$ and $O_2$ used in the manuscript were optimized with the SMD implicit solvation model.

We considered different sizes of Co clusters and found the planar $Co_7O_{24}H_{27}$ cluster with edge-sharing $CoO_6$ octahedral is the most stable structure, which is consistent with the structure model suggested by EXAFS study.[12] We considered different protonation state of the $Co_7O_{24}H_{27}$ cluster by placing protons at different O positions and found the most stable configuration corresponds to protonated $\mu_2$-O and $\mu_3$-O bridges, which was used for our mechanistic investigation. We simulated the O-O vibrational frequency of the O-O bond in possible intermediates. We used the atomic masses of specified isotopes and diagonal the Hessian matrix in the mass-weighted coordinates to obtain the vibrational frequency for different isotopes.

The free energy changes of proton-coupled electron transfer steps were calculated with Nørskov's computational hydrogen electrode (CHE) approach[13] to get the free energy change with respect to the reversible hydrogen electrode (RHE) to avoid the explicit use of the hydrated proton and to include the pH effect naturally. Its procedure is given below:

1. Calculate the free energy change ($\Delta G_1$) with respect to the release of ½ equivalence of $H_2$(g):

$$RH \rightarrow Ox + \frac{1}{2}H_2(g), \Delta G_1$$

2. Use the definition of RHE:

$$\frac{1}{2}H_2(g) \rightarrow H^+(aq) +\ e^-, \Delta G_2$$

3. Free energy change of a proton-coupled electron transfer step ($\Delta G_3$) with respect to RHE can be calculated by adding $\Delta G_1$ and $\Delta G_2$:

$$RH \rightarrow Ox + H^+ + e^-, \qquad \Delta G_3 = \Delta G_1 + \Delta G_2$$

We also considered the water oxidation mechanisms on CoOOH. Given the nature of this system, we applied periodic boundary condition to study the catalytic mechanism on CoOOH surfaces. All calculations for the CoOOH system were performed with the Vienna Ab initio Simulation Package (VASP).[14,15,16,17] We use the Perdew-Burke-Ernzerhof (PBE) exchange-correlation functional[18] in conjugation with the projected-augmented wave (PAW) method[19,20] to describe the ion-electrons interactions. A cutoff energy of 500 eV was chosen for the plane wave basis set in all calculations. We used the Gaussian smearing method to accelerate SCF convergence and the σ value was chosen to be 0.1 eV. The standard GGAs fail for strongly correlated systems such as the d electrons of Co. All calculations involving Ir and Ce atoms were performed with the spin-polarized DFT+*U* method, using the rotational-invariant formalism developed by Dudarev et al.[21] The empirical $U_{eff}$ parameters were chosen to be 3.4 eV for Co 3d electrons.[22]

A 9 × 9 × 9 Monckhorst-Pack type k-point grid[23] was chosen for the optimization of bulk ceria. The energy convergence criterion was set to be $10^{-6}$ eV per unit cell and the geometry convergence criterion was set to be $10^{-5}$ eV per unit cell for energy difference between two consecutive ionic steps. The optimized lattice constants $a = b = 2.88$ Å and $c = 13.17$ Å are in good agreement with experimental lattice constant of $a = b = 2.85$ Å and $c = 13.15$ Å.[24]

We prepared slab models for the CoOOH (012) surface to study the water oxidation mechanisms on the the CoOOH (012) surface. CoOOH (012) surface with 3 layers of Co atoms with both sides terminated by water ligands are used in the study (Figure S21). A vacuum layer of ~ 15 Å was used to minimize the artificial interactions between periodic images. A supercell of 13.52 Å × 31.54 Å × 14.37 Å was used to model the CoOOH (012) surface. The atoms in the bottom one layers were fixed at their optimized positions, while the atoms in the top two layers, as well as the adsorbates, were allowed to relax during geometry optimization. A 1 × 1 × 1 Monckhorst-Pack type k-point grid was used for all surface structure relaxations unless otherwise noted. The energy convergence criterion was set to be $10^{-5}$ eV per super cell and the force convergence criterion of 0.03 eV $Å^{-1}$.

The calculations of isolated small molecules were performed with a supercell of 15.0 Å × 15.0 Å × 15.0 Å. The Gaussian smearing method and a σ value of 0.1 eV were used in the calculations. A 1 × 1 × 1 Monckhorst-Pack type k-point grid was used to sample the Brillouin zone and the SCF convergence criterion was set to be $10^{-5}$ eV per unit cell.

The energy changes obtained from the periodic boundary calculations were corrected by the thermo-correction from the cluster model to obtain the free energy changes given in Figure S27. The saturated vapor pressure of water at 298.15 K (3.169 kPa) was used to obtain the free energy changes of $H_2O(g) \rightarrow H_2O(l)$.

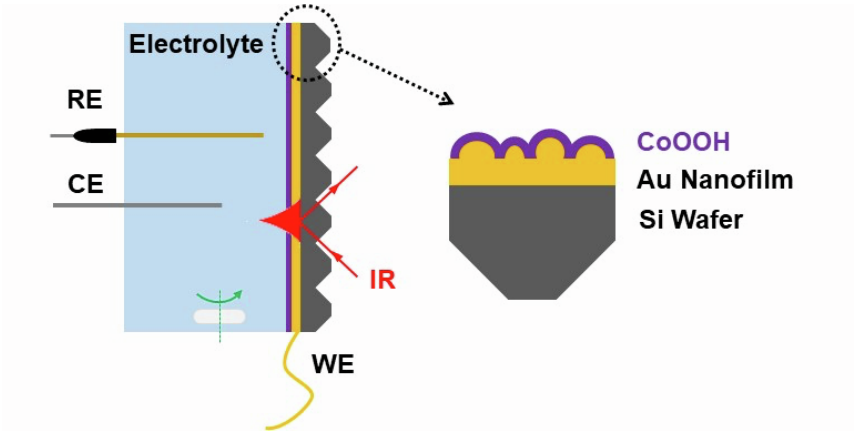


**Figure S1. Experimental configuration for SEIRAS.** WE, CE, and RE denote the working electrode, counter electrode, and reference electrode, respectively.

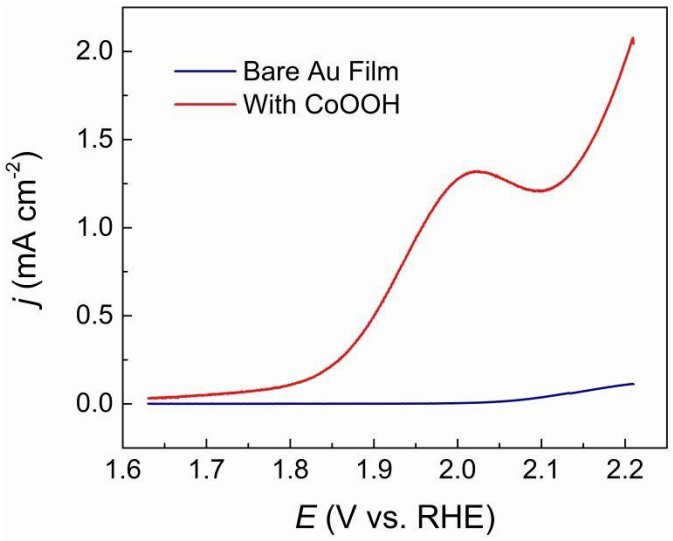


**Figure S2. Water oxidation activity comparison between bare Au film and $CoO_x(OH)_y$-Au sample**. The CVs were collected from 1.61 to 2.21 V at a scan rate of 20 mV $s^{-1}$. The current data are from the third forward scan of the catalyst. All the data were corrected with *iR* compensation.

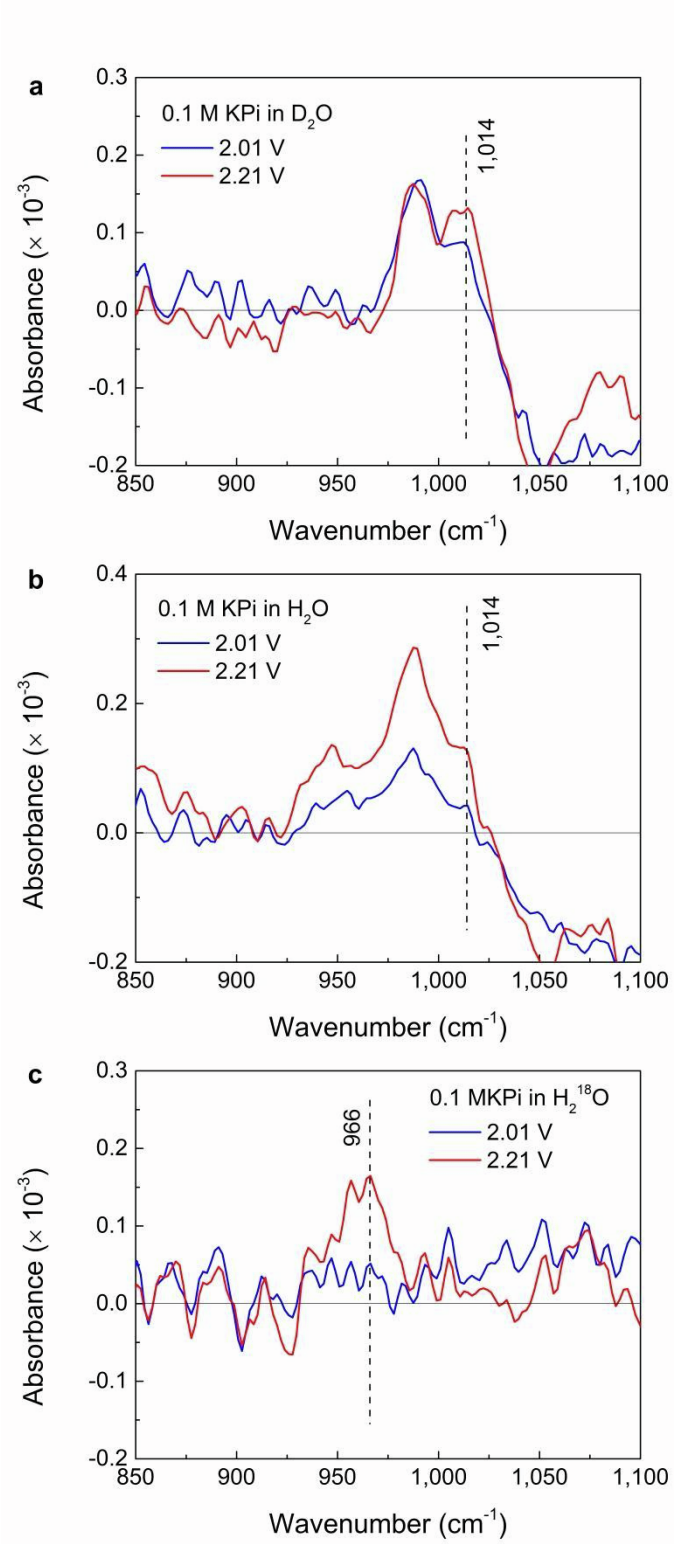


**Figure S3. Potential-dependence of the band centered at 1,014 cm$^{-1}$.** The intensity of the band centered at 1,014 cm$^{-1}$ at 2.21 V increases with increasing applied potential in 0.1 M KPi with (**a**) $D_2O$, (**b**) $H_2O$, and (**c**) $H_2{}^{18}O$.

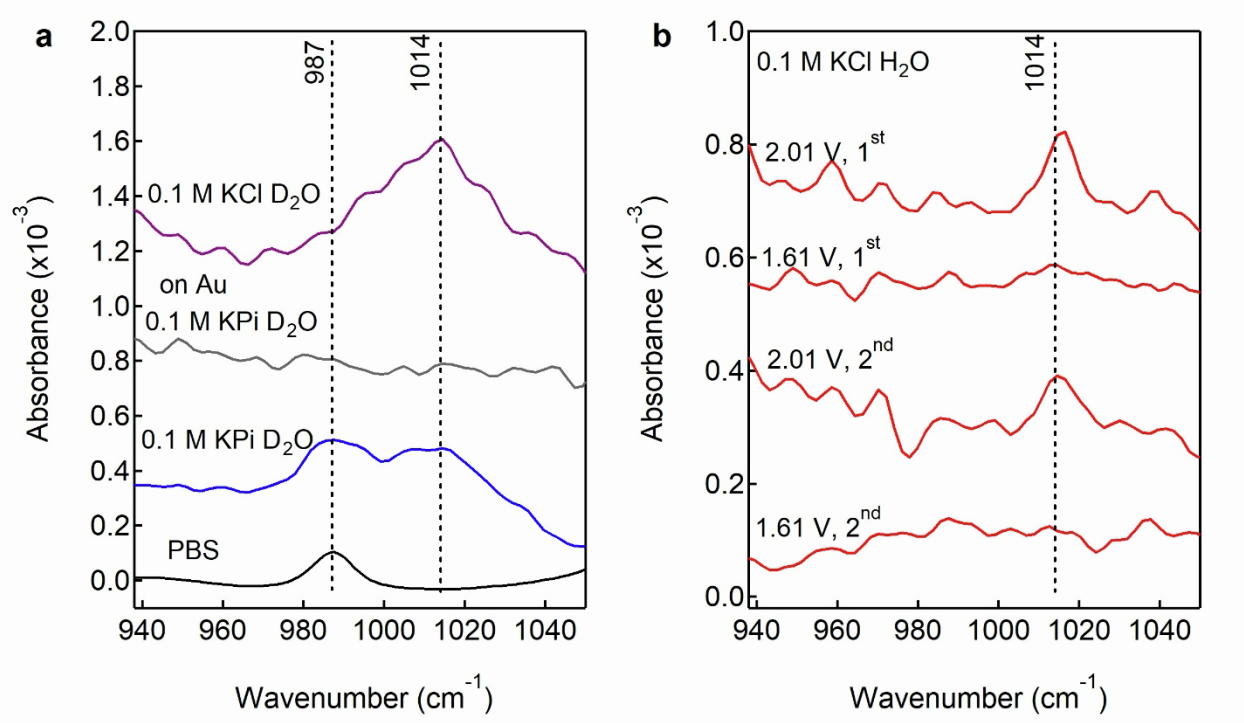


**Figure S4. Control experiments for ruling out the complication brought up by solution species.** (**a**) A prominent band at 1,014 $cm^{-1}$ is observable in 0.1 M KCl with $D_2O$ at 2.21 V, while the band does not appear on a bare Au at the same potential. PBS indicates the spectrum of a bulk phosphate solution. (**b**) The band at 1014 $cm^{-1}$ shows a potential-dependent reversibility as potential is switched between 2.01 V and 1.61 V (two cycles are shown labeled as "$1^{st}$" and "$2^{nd}$").

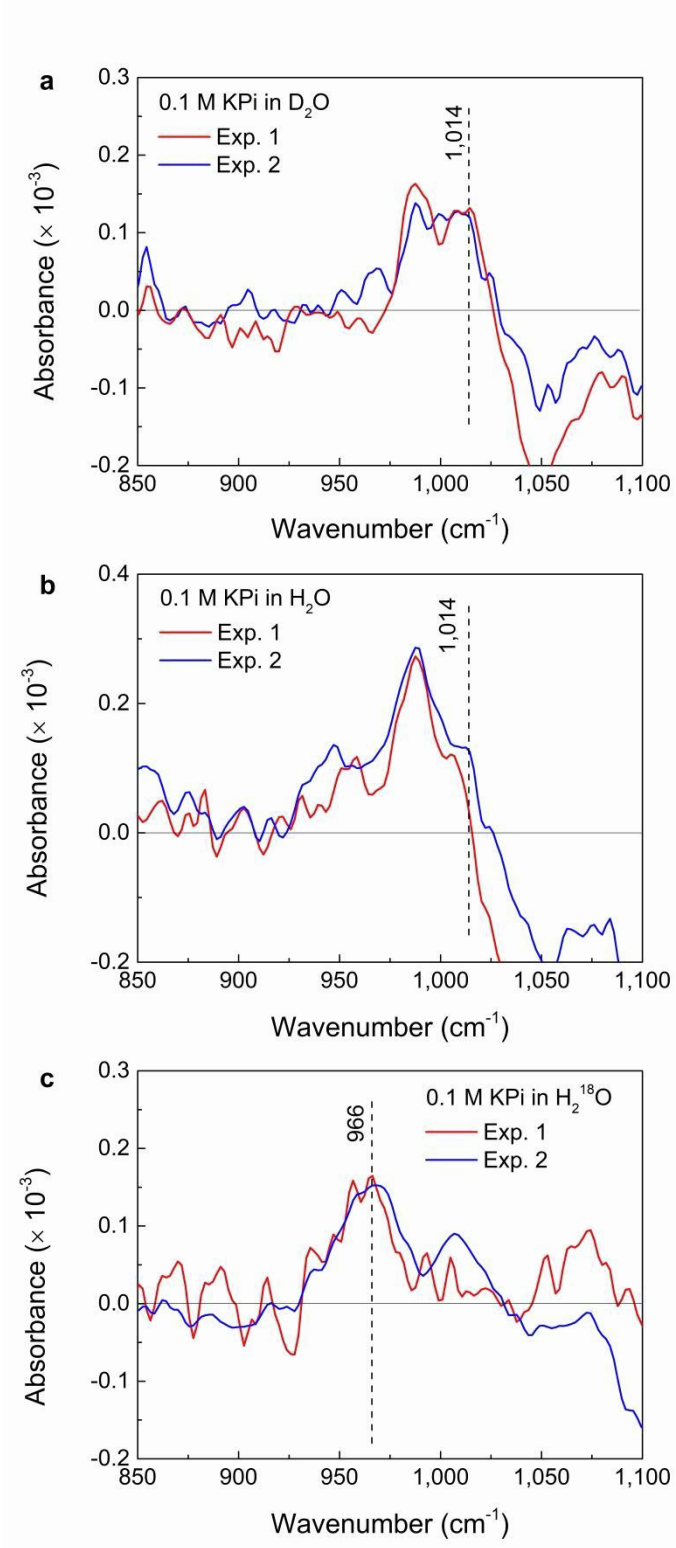


**Figure S5. SERIAS experiment is reproducible.** SEIRAS data collected on different samples in 0.1 M KPi with (**a**) $D_2O$, (**b**) $H_2O$, and (**c**) $H_2{}^{18}O$, to demonstrate reproducibility at 2.21 V. Reference spectra were taken at 1.61 V.

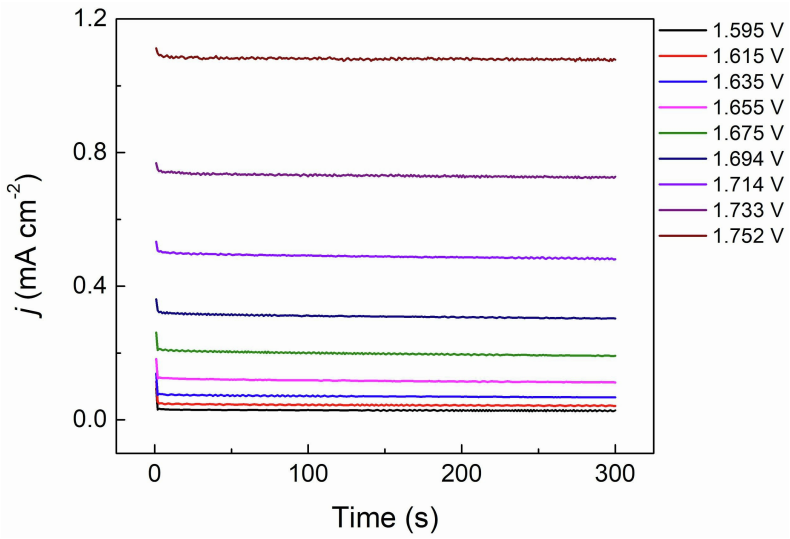


**Figure S6. Representative steady-state electrochemical *j-t* plots of water oxidation on Co-Pi catalysts.** Current was collected in 0.1 M KPi containing 2 m $NaNO_3$ electrolyte ($a_w$= 0.94) at various potentials as indicated. The electrode potential was corrected for the *iR* drop.

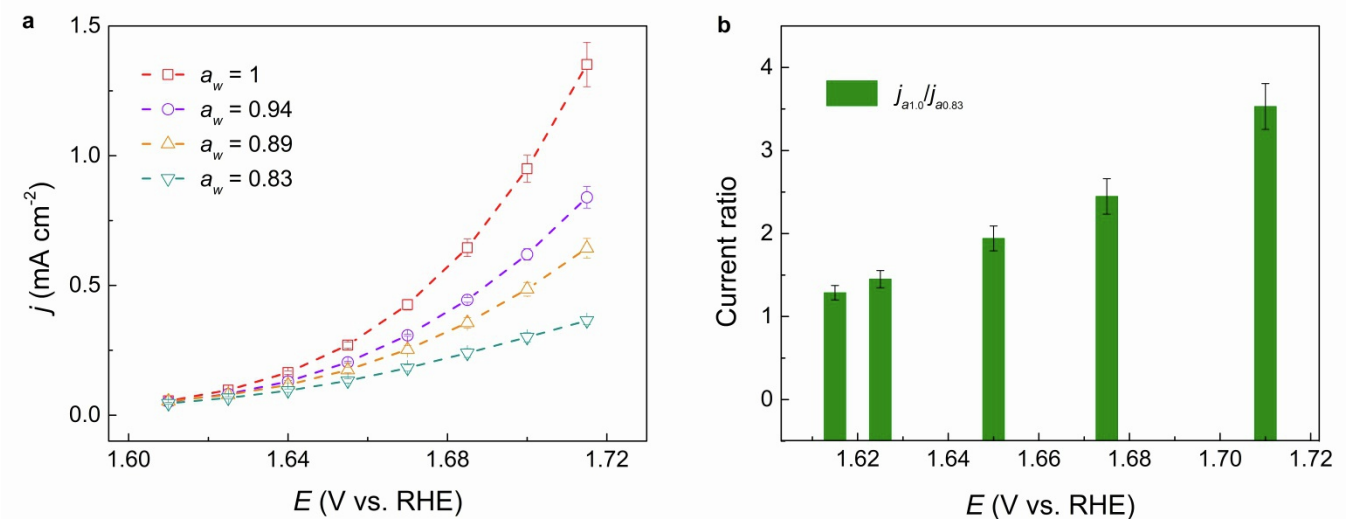


**Figure S7. Potential-dependence of the current modulation ratio for different water activities on $CoO_x(OH)_y$.** Steady-state water oxidation current density as in **Figures 3a** and **3b**, but collected on a $CoO_x(OH)_y$-coated Pt electrode under stirring condition. The data were derived from an average of three independent experiments for each $a_w$. Error bars denote the standard deviation of three individual measurements. Error bars denote the standard deviation of three individual measurements. The electrode potential was corrected for the *iR* drop.

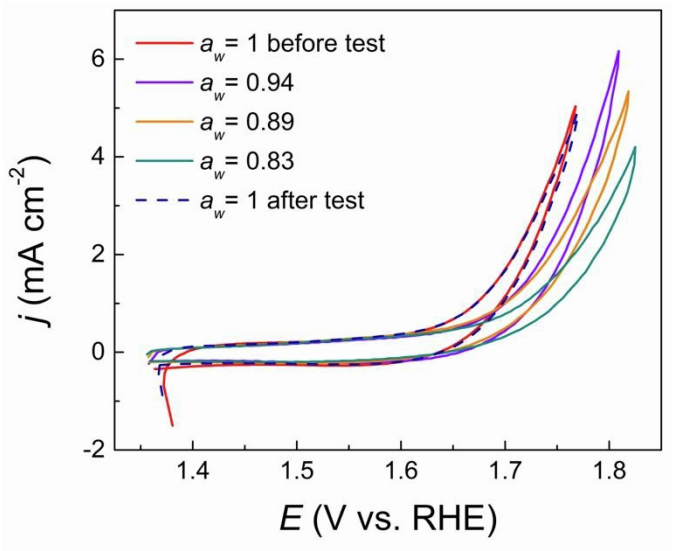


**Figure S8. CV stability test of the Co-Pi catalyst.** CV stability test of the same Co-Pi catalyst before and after a series of CVs in water-in-salt electrolytes at a scan rate of 20 mV $s^{-1}$. The CV measurements are from the first cycle of the catalyst. The electrode potential was corrected for the *iR* drop.

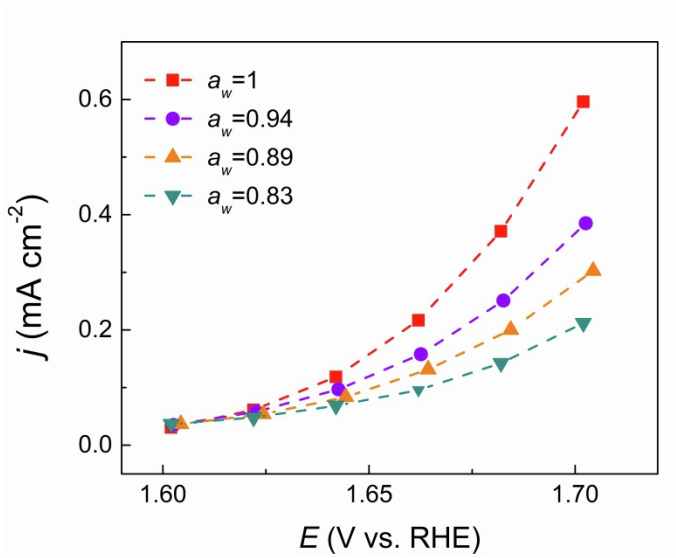


**Figure S9. Control experiments for ruling out mass transport limitation.** Steady-state water oxidation current density as in **Figure 3a**, but collected on a Co-Pi-coated Pt RDE at a rotation rate of 2,000 rpm. The electrode potential was corrected for the *iR* drop.

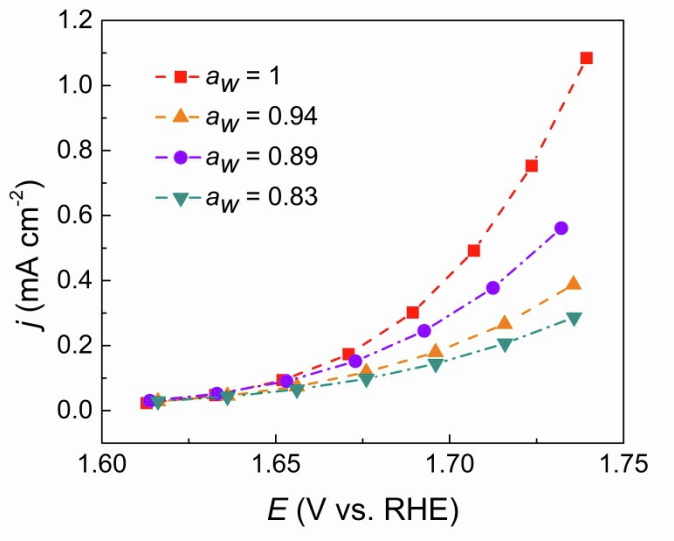


**Figure S10. Control experiments for ruling out substrate effect.** Steady-state water oxidation current density on a Co-Pi-coated Pt RDE as that in **Figure S9** but collected at a rotation rate of 0 rpm. The electrode potential was corrected for the *iR* drop.

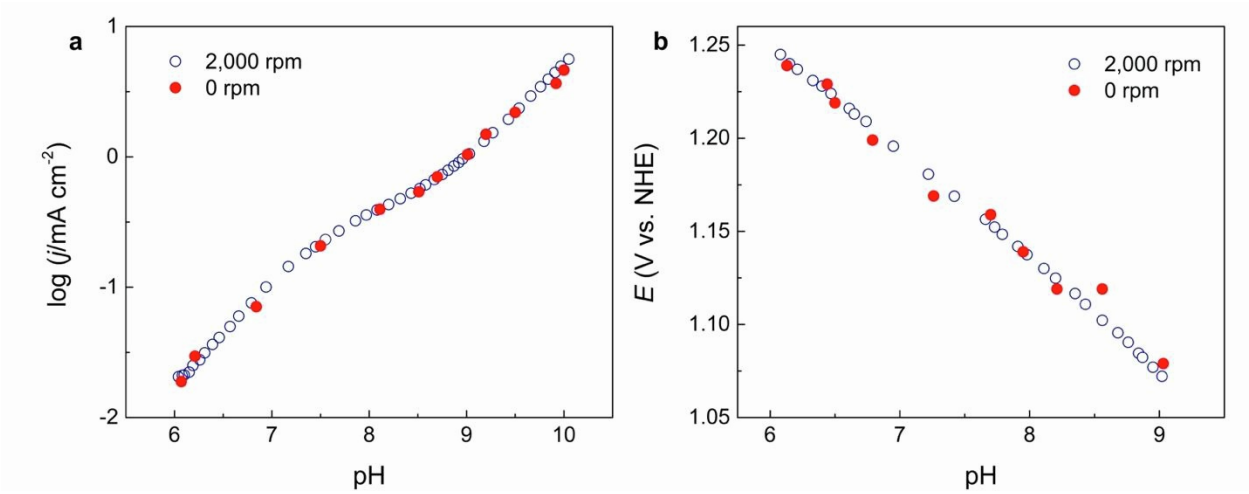


**Figure S11. pH titration experiments in 2 m $NaNO_3$ electrolyte.** pH titration under (**a**) controlled-potential (1.237 V vs. NHE) and (**b**) controlled-current (30 μA $cm^{-2}$) for a Co-Pi-coated Pt RDE in 2 m $NaNO_3$@0.1 M KPi ($a_w$= 0.94) at two different rotation rates, as indicated. These data were collected under steady state conditions.

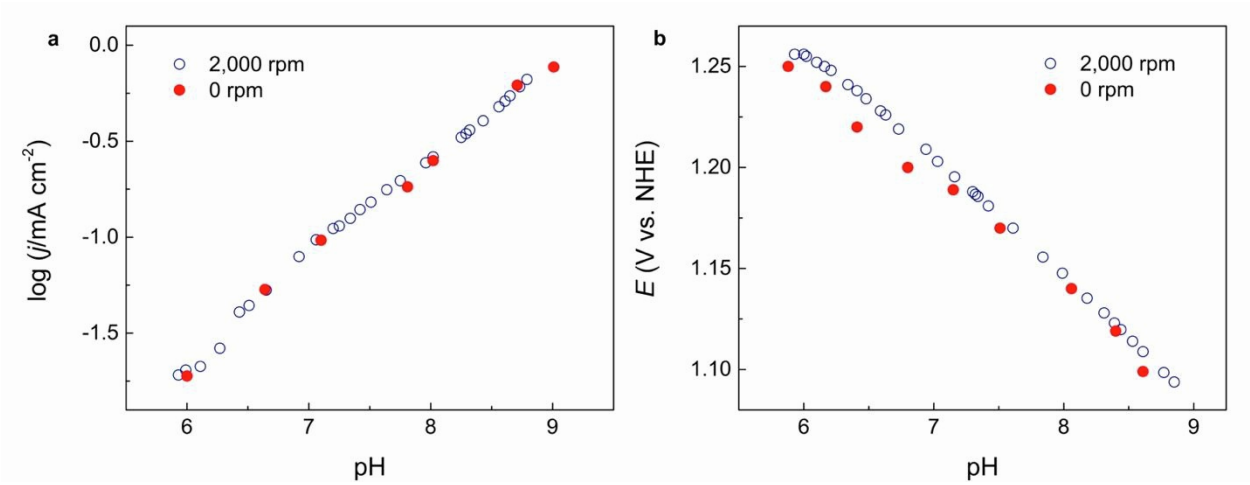


**Figure S12. pH titration experiments in 4 m $NaNO_3$ electrolyte.** pH titration under (**a**) controlled-potential (1.237 V vs. NHE) and (**b**) controlled-current (30 μA $cm^{-2}$) for a Co-Pi-coated Pt RDE in 4 m $NaNO_3$@0.1 M KPi ($a_w$= 0.89) at two different rotation rates, as indicated. These data were collected under steady state conditions.

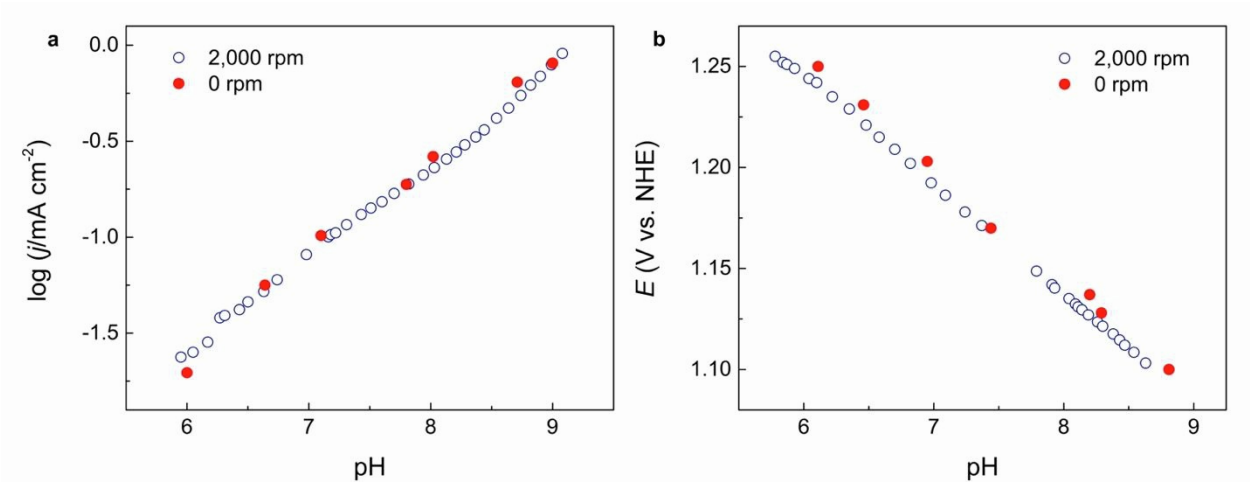


**Figure S13. pH titration experiments in 7 m $NaNO_3$ electrolyte.** pH titration under (**a**) controlled-potential (1.237 V vs. NHE) and (**b**) controlled-current (30 μA $cm^{-2}$) for a Co-Pi-coated Pt RDE in 7 m $NaNO_3$@0.1 M KPi ($a_w$= 0.83) at two different rotation rates, as indicated. These data were collected under steady state conditions.

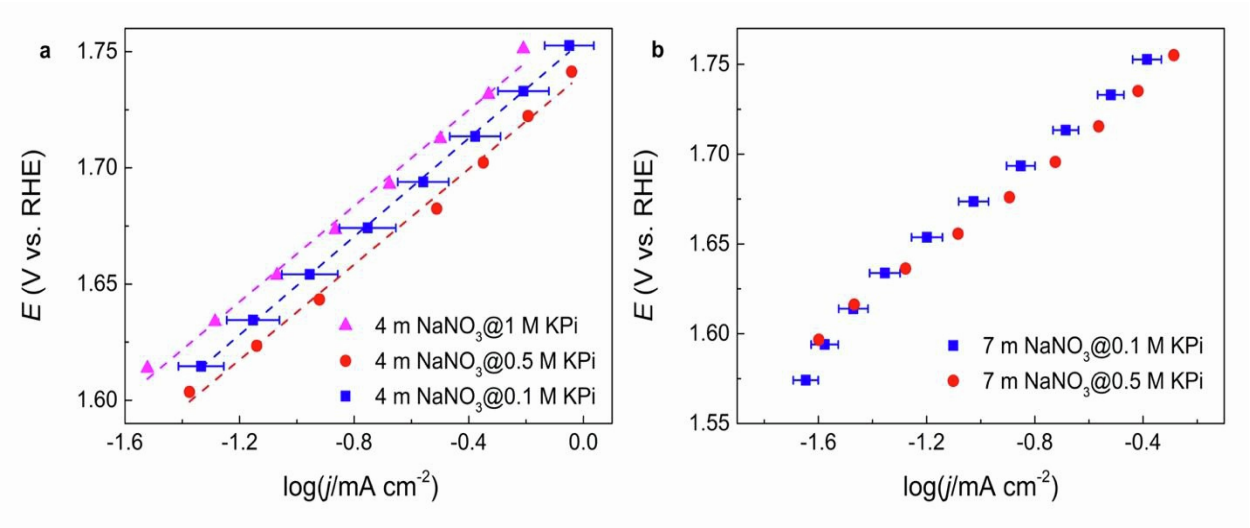


**Figure S14. Tafel data for different buffer concentrations.** Tafel data for (**a**) 4 m $NaNO_3$ (**b**) 7 m $NaNO_3$ containing different concentrations of KPi indicate that there is no significant dependence of the slope and reaction rate on KPi concentration. These data were collected under steady state conditions. The electrode potential was corrected for the *iR* drop. Error bars denote the standard deviation of three independent measurements.

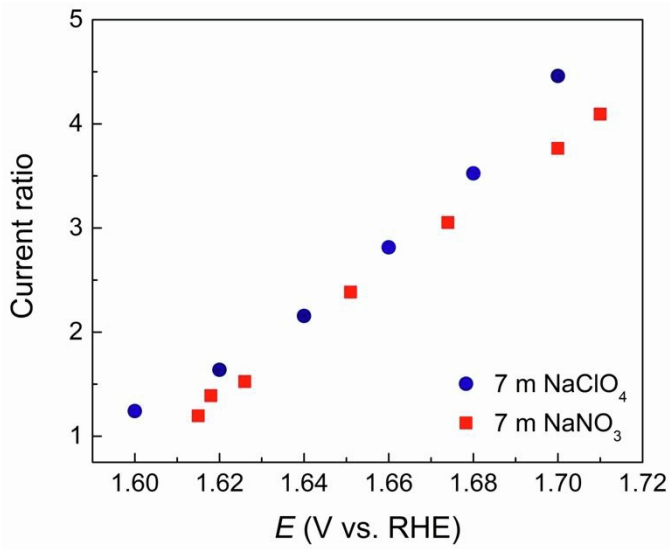


**Figure S15. Control experiments for ruling out anion effect.** To study the influence of the anion on the electrocatalytic activity, we replaced $NaNO_3$ with $NaClO_4$ to perform a similar potentiostatic measurement. The buffer solution was 0.1 M NaPi to avoid precipitation of $KClO_4$. These data were collected under steady state 0.2 M conditions. The electrode potential was corrected for the *iR* drop.

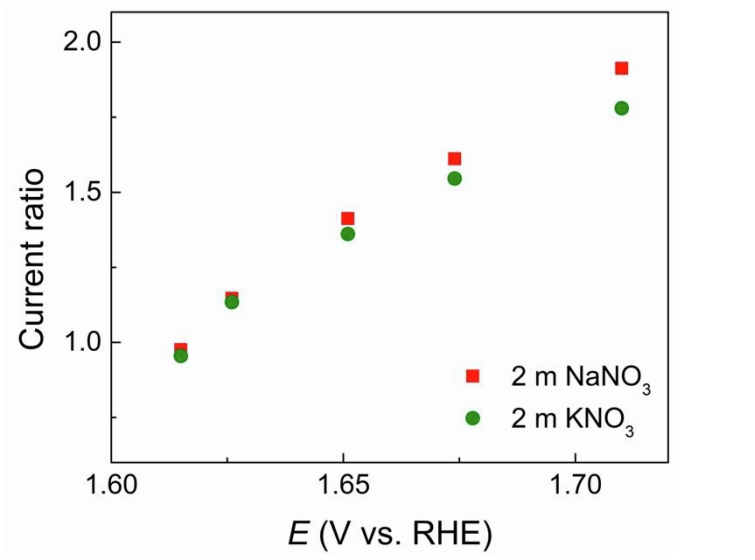


**Figure S16. Control experiments for ruling out cation effect.** Current modulation ratios in $a_w$ = 0.94 with different cations. The concentration is limited by the $KNO_3$ solubility. These data were collected under steady-state conditions. The electrode potential was corrected for the *iR* drop.

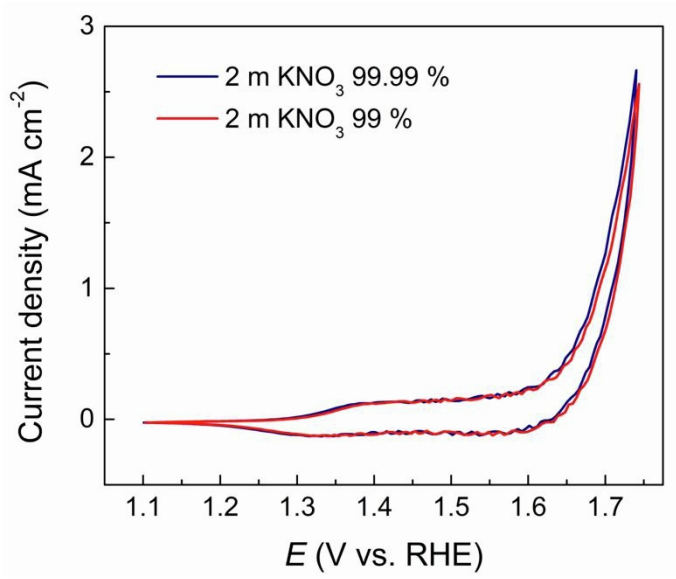


**Figure S17. Control experiments for ruling out impurity effect.** Comparison of CV data collected in 2 m 99% $KNO_3$ and 2 m 99.99% $KNO_3$ at a scan rate of 20 mV $s^{-1}$. The CV measurements are from the third cycle of the catalyst. The electrode potential was corrected for the *iR* drop.

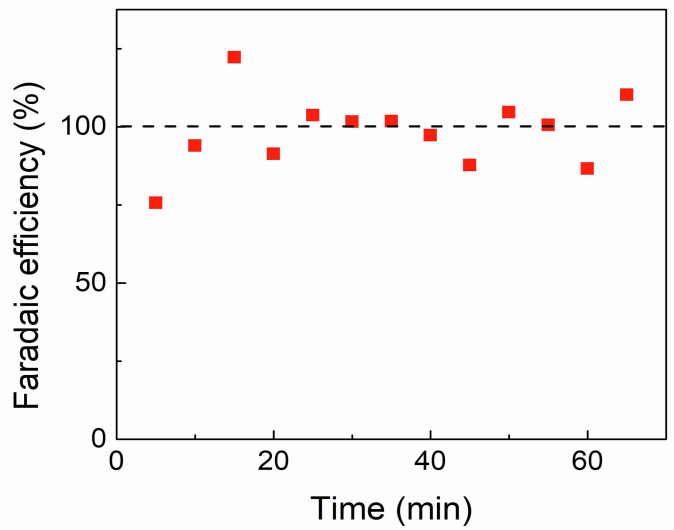


**Figure S18. The faradaic efficiency for $O_2$.** The faradaic efficiency for $O_2$ was measured at a current of 3 mA in 7 m $NaNO_3$ solution containing 0.1 M KPi buffer with gas chromatography.

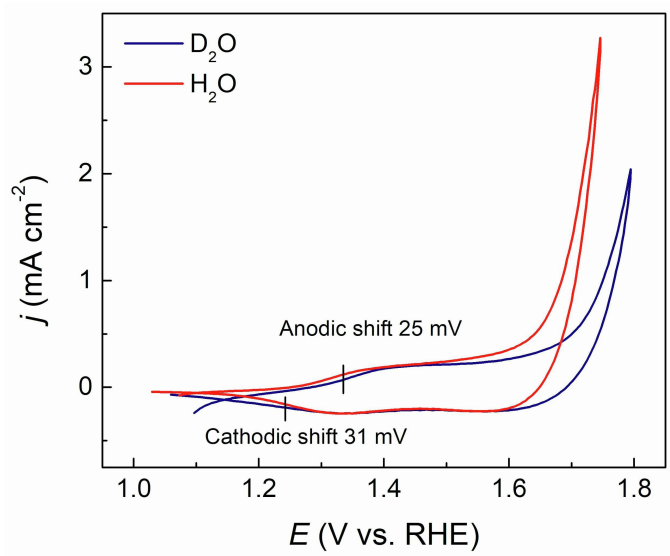


**Figure S19. Comparison of CV data collected in $D_2O$ and $H_2O$.** The scan rate is 20 mV $s^{-1}$. The electrode potential was corrected for the *iR* drop. The CV measurements are from the first cycle of the catalyst. The shift of the half-wave potential was calculated according to the following equation:

$$\text{Shift of redox half wave potential} = \frac{\text{Shift of anodic feature} + \text{Shift of cathodic feature}}{2}$$

$$= \frac{25\ \text{mV} + 31\ \text{mV}}{2} = 28\ \text{mV}$$

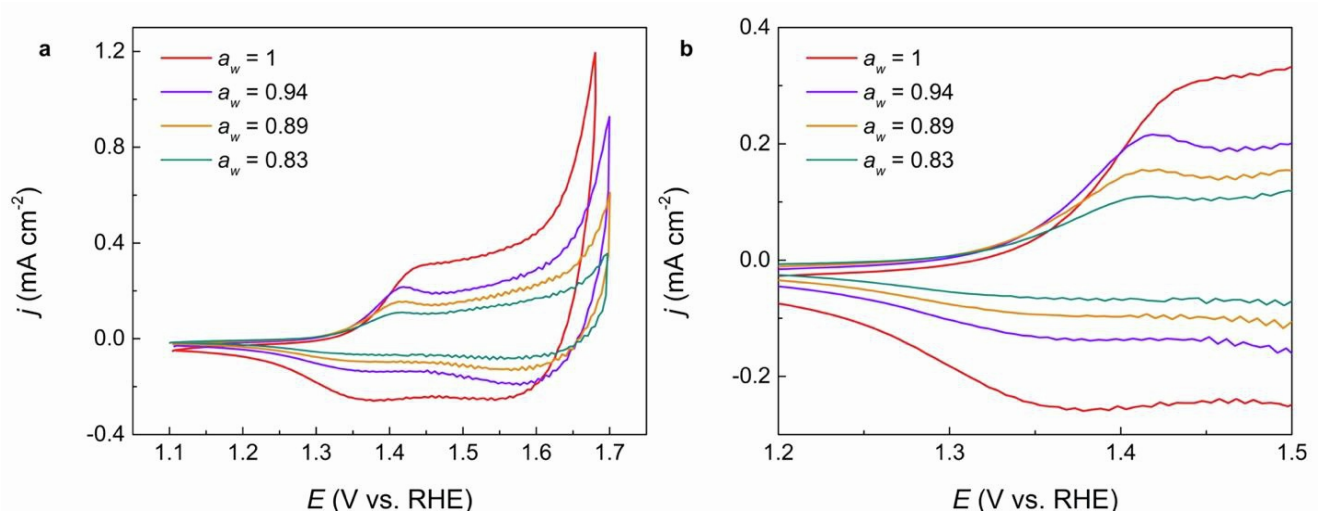


**Figure S20. A series of CVs of the Co-Pi catalyst in water-in-salt electrolytes.** The scan rate is 20 mV $s^{-1}$ in (**a**) full range and (**b**) zoomed range. The CV measurements are from the third cycle of the catalyst. The electrode potential was corrected for the *iR* drop.

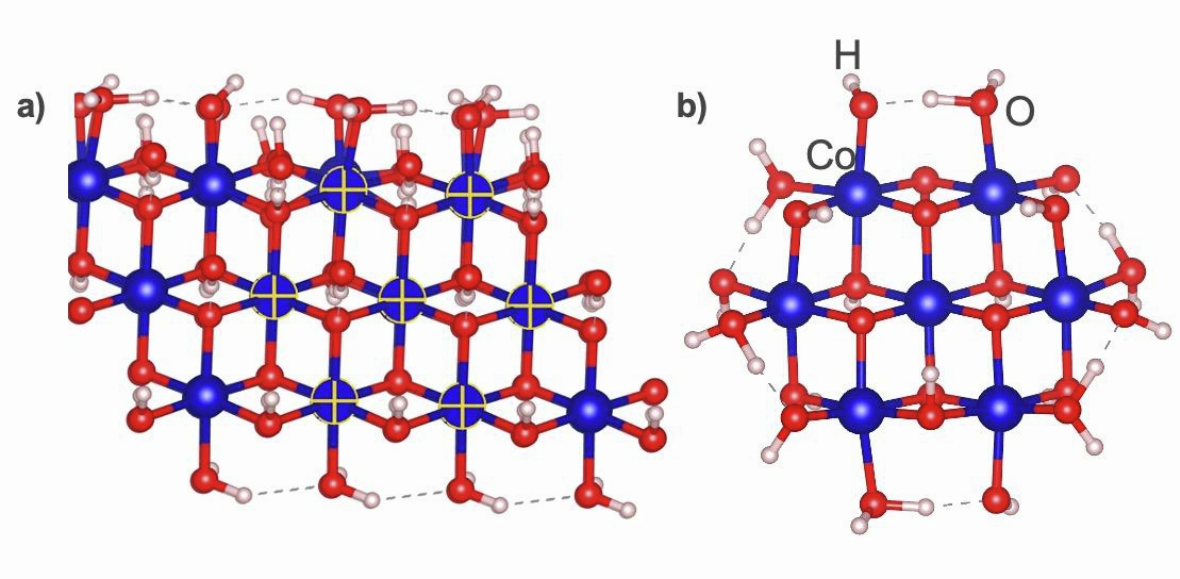


**Figure S21. The structural models of (a) the CoOOH (012) surface and (b) the Co-Pi catalyst.** The cluster model of the Co-Pi catalyst is based on previous EXAFS study.[12] The Co7 core in the cluster model resemble the highlighted Co7 unit in the CoOOH structure. The atomic model of Co cluster ($Co_7O_{24}H_{27}$) is constructed for our theoretical study with the water and hydroxides ligands. The blue, red, and white spheres represent Co, O, and H atoms, respectively.

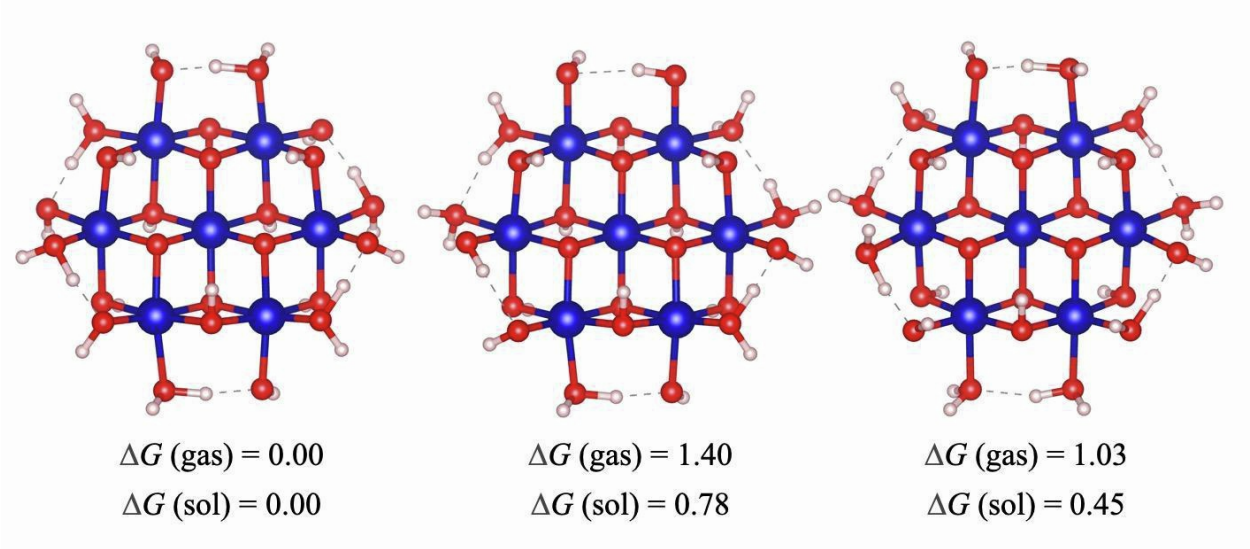


**Figure S22. Relative free energies of the $Co_7O_{24}H_{27}$ cluster with different protonation states in gas phase and in aqueous solution.** The most stable protonation state (left) has alternative HO---$H_2O$ hydrogen bond interactions at peripheric Co pairs and the bottom $\mu_3$-O bridges being protonated. Destroying the alternative HO---$H_2O$ hydrogen bond interaction by preparing $H_2O$---$H_2O$ and HO---HO hydrogen bonding pattern increases the energy (middle). Removing the protons from $\mu_3$-O bridges to terminal $OH^-$ increases the energy (right) since it disturbs the strong HO---$H_2O$ hydrogen bond interactions. We choose the most stable protonation state (left) for our mechanistic study. It is worth pointing out that the free energy different in the solution is much smaller than in the gas phase due to a large geometry relaxation due to the high dielectric solvation environment. Therefore, we optimized all geometries in the SMD implicit solvation model.

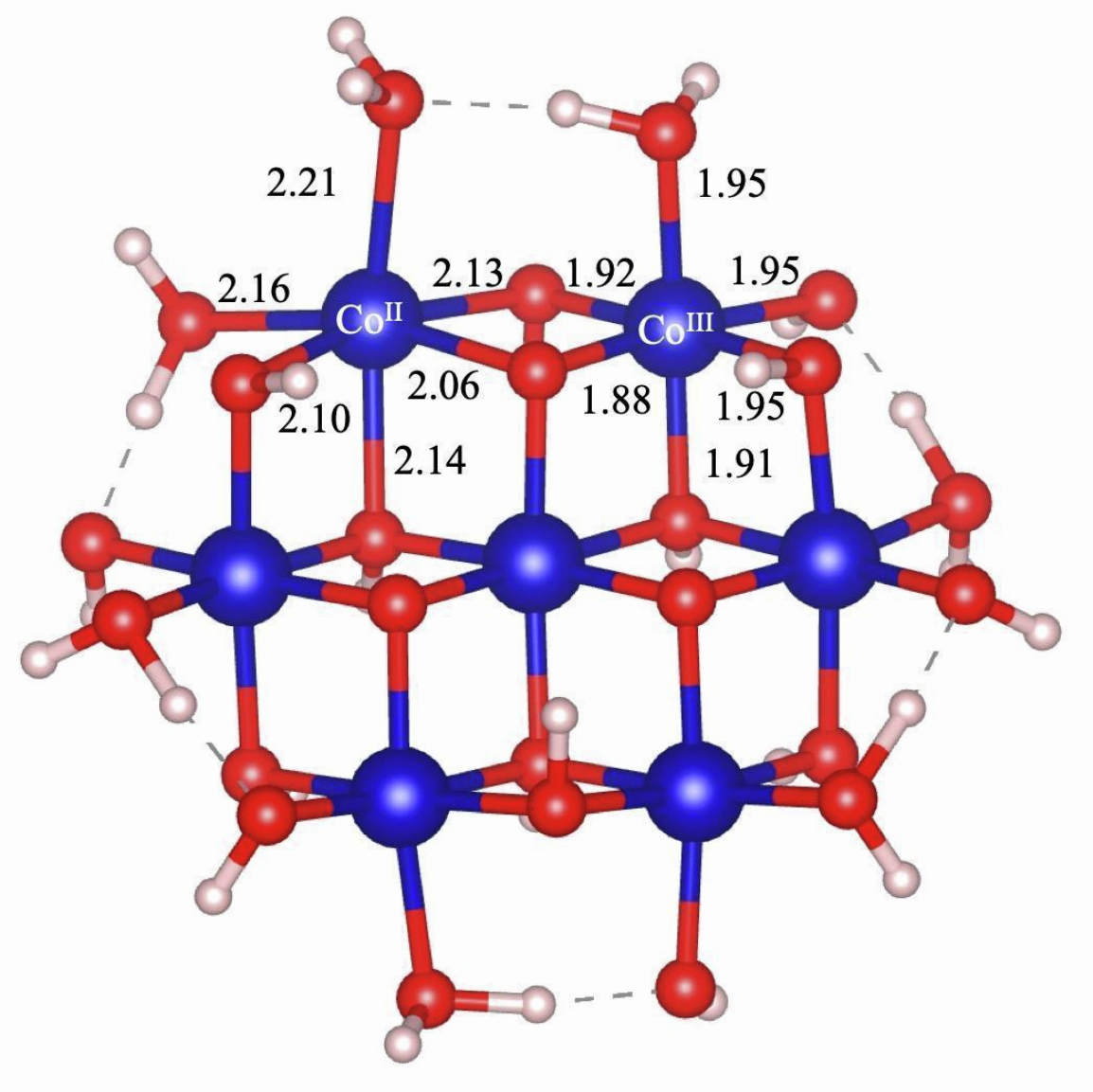


**Figure S23. Optimized Co–O bond lengths around the Co(II) and Co(III) centers in intermediate I.** The Co–O bond lengths are somewhat longer around the Co(II) center since the ground state of Co(II) is a high-spin quartet. In contrast, the low-spin Co(III) center has much shorter Co–O bond lengths and stronger metal-ligand interactions which are crucial for the stability of the molecular-like Co-Pi water oxidation catalyst.

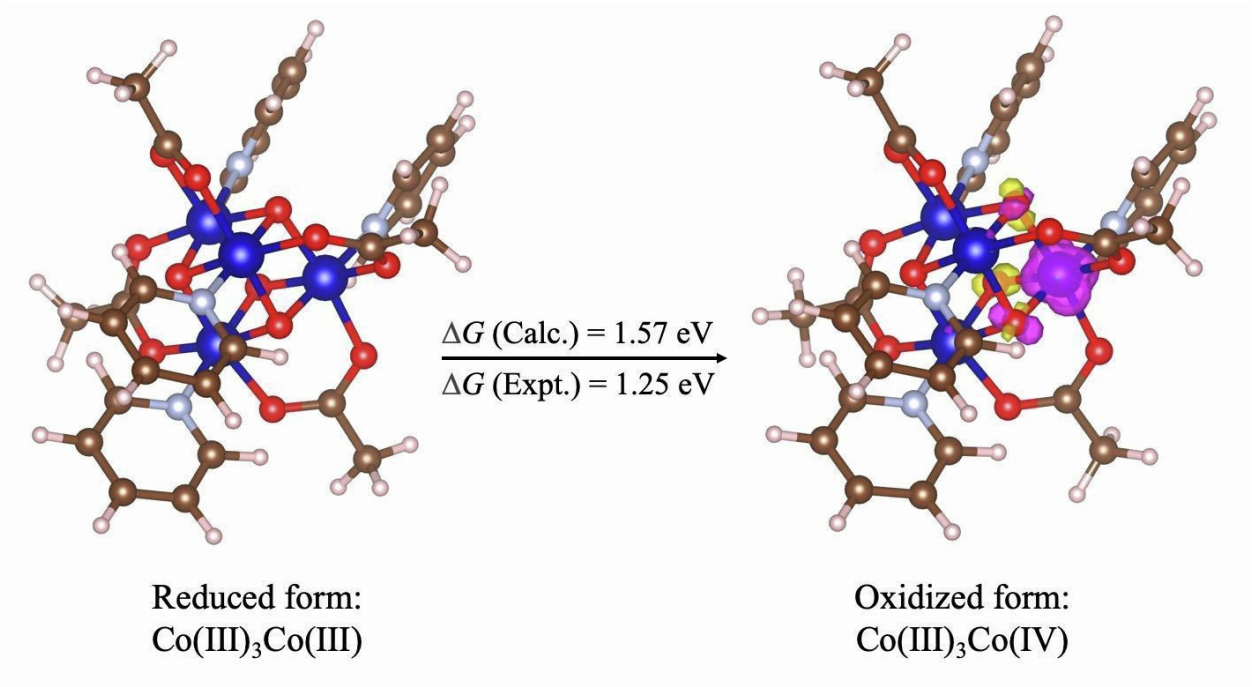


**Figure S24. Optimized structures of the $Co_4O_4(OAc)_4(Py)_4$ complex in its reduced and oxidized form.** Magenta and yellow isosurfaces show the alpha and beta spin density distribution and are plotted with an isovalue of 0.01 $Å^{-3}$. The calculated and experimental[25] free energy changes with respect to the normal hydrogen electrode (NHE) are 1.57 and 1.25 eV, respectively. Our calculation using the B3LYP functional overestimates the potential for oxidation potential of Co(III) to Co(IV) by 0.3 eV, which is consistent with a recent benchmark study,[26] highlighting the difficulty to describe the high oxidation Co complex.

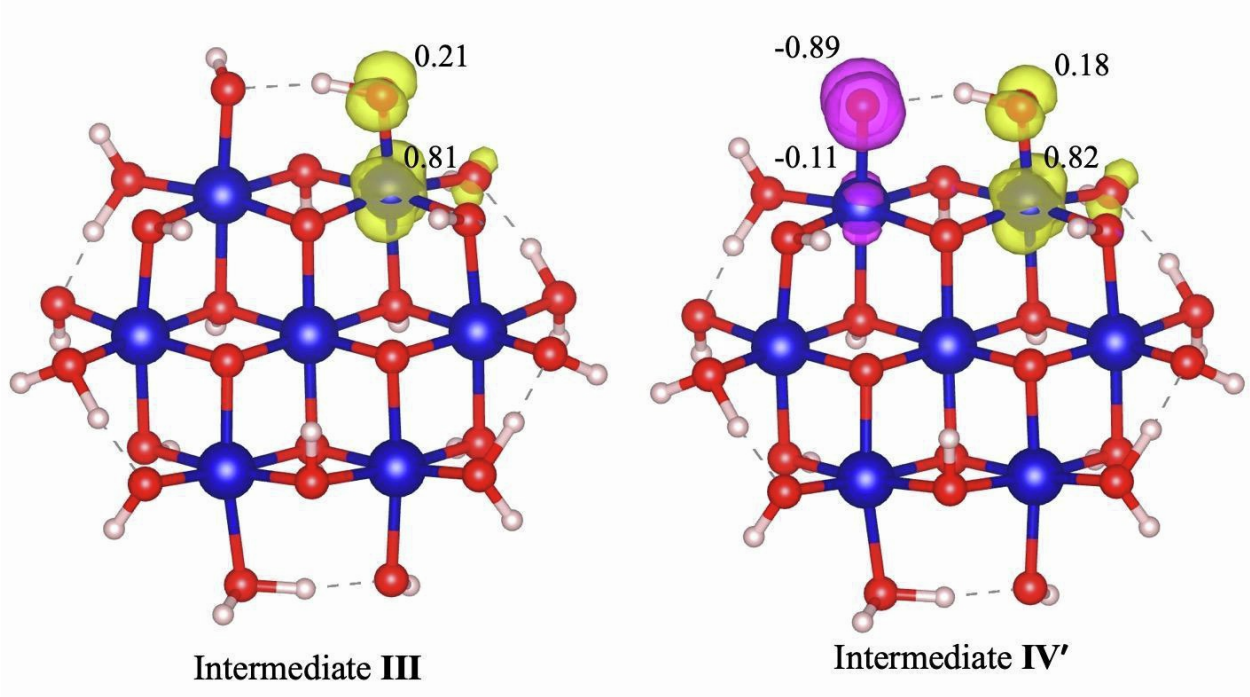


**Figure S25. Optimized structures of intermediates III and IV′.** Magenta and yellow isosurfaces show the alpha and beta spin density distribution and are plotted with an isovalue of 0.01 $Å^{-3}$. The numbers next to Co and O ions indicate their Mulliken spin density population. It can be seen clearly that the $OH^-$ coordinated to the Co(IV) center has significant radical character while the Co(IV)=O in intermediate **IV′** is best described as Co(III)–O$^{\bullet}$.

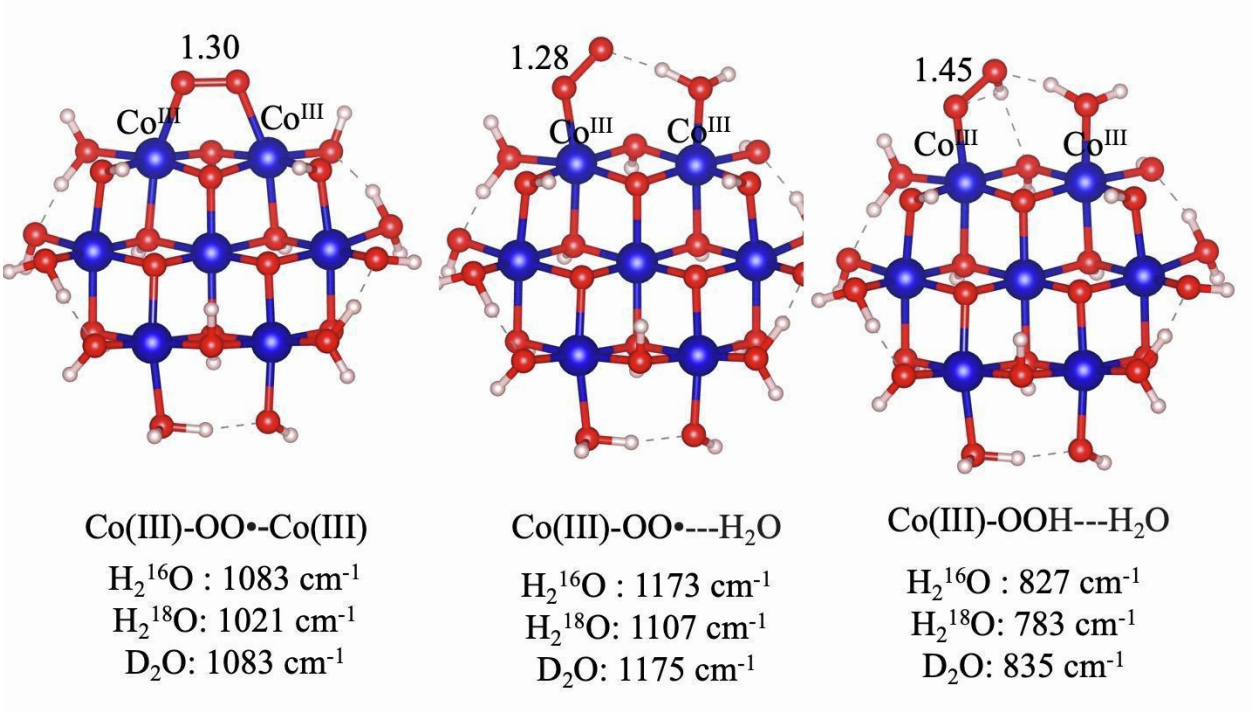


**Figure S26. Calculated O–O vibrational frequencies and associated isotope shifts for possible intermediates.**

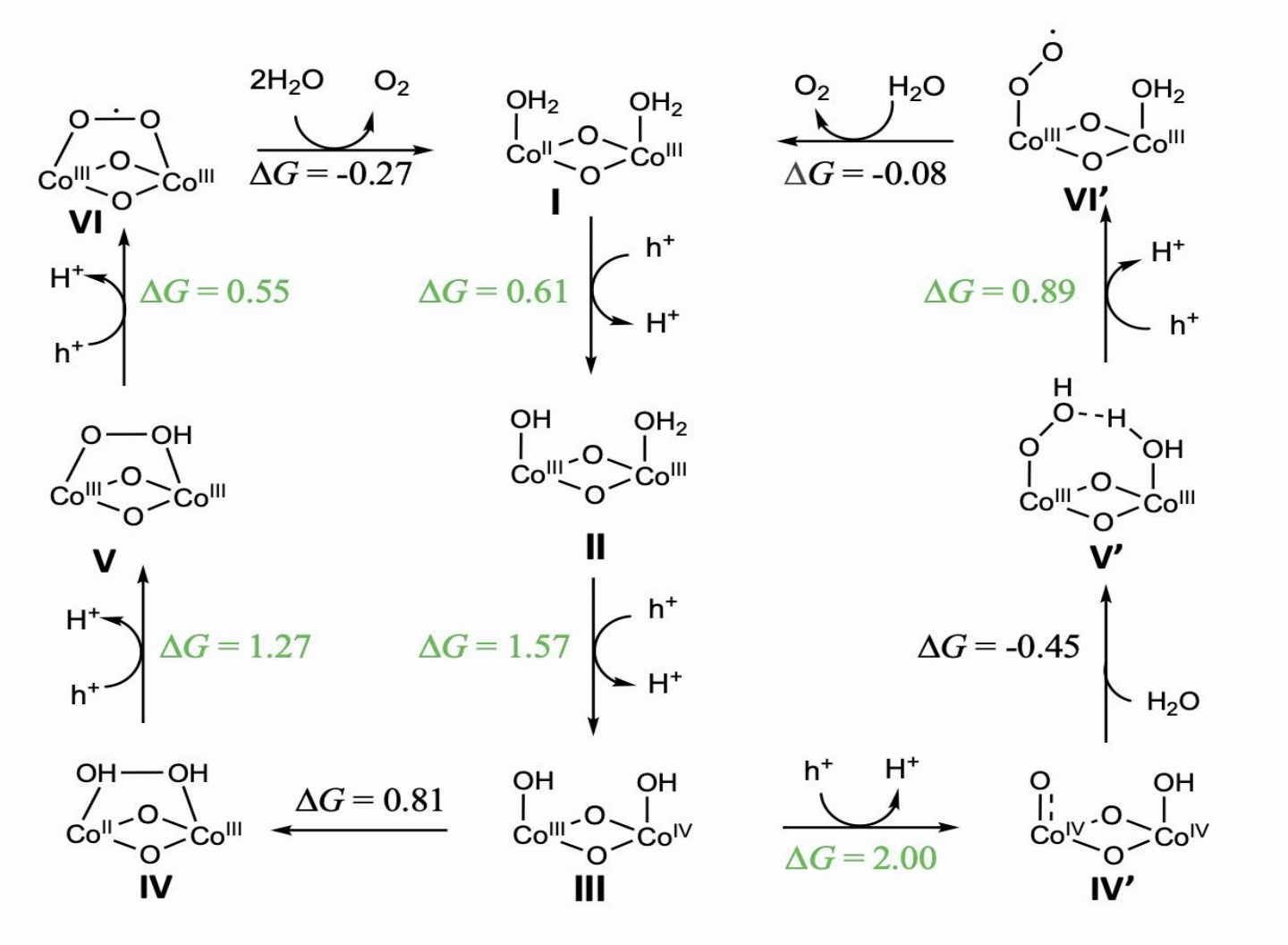


**Figure S27. Possible routes of water oxidation on the CoOOH (012) surface suggested by the DFT calculations.** Similar to the results of Co-cluster model for Co-Pi system, the IMOC mechanism is possible under low applied potential while the WNA mechanism require higher potential to be accessible. The calculated free energy changes ($\Delta G$) are given in the unit of eV. The numbers shown in green are the free energy changes of electrochemical steps vs. the computed hydrogen electrode.

**Table S1. Viscosities ($\eta$), densities ($d$), and stagnant layer thickness ($y_s$) of water-in-salt electrolytes.**

| $m$ (mol/kg) | $\eta$ (cP ) | $d$ (g/mL) | $y_s$ at $f$ =2000 rpm (μm) |
|---|---|---|---|
| 0[a] | 1 | 1 | 249 |
| 2.14[b] | 1.04 | 1.11 | 241 |
| 3.32[b] | 1.19 | 1.16 | 252 |
| 4.62[b] | 1.30 | 1.21 | 258 |
| 6.02[b] | 1.62 | 1.26 | 283 |
| 7.56[b] | 1.92 | 1.30 | 302 |

[a] Based on the assumption that the viscosity and density of 0 m solution are 1 cP and 1g/mL.
[b] Based on Ref (28)

The stagnant layer thickness ($y_s$) is calculated based on

$$y_s = 3.6 \times \left(\frac{\upsilon}{\omega}\right)^{\frac{1}{2}}$$

where $\upsilon = \frac{\eta}{d}$ is the kinematic viscosity, and $\omega = \frac{2\pi f}{60}$ is the angular rotation rate at $f$ (rotation rate in revolutions per minute).[27]

The viscosity of water-in-salt solutions are expected to increase from 1 to ~ 2 cP when increasing the molality from 0 to 7.56 m.[28] The stagnant layer thicknesses at all molalities fall in the range of 200-300 μm, which are expected for conventional RDE measurements at a rotating rate of 2000 rpm. The thickness first decreases with the addition of high molality salt, then it increases as the molality increases. When the molality increases from 2 to 7.56 m, the thickness increases ca. 25%.

## References


1. Miyake, H.; Ye, S.; Osawa, M. (2002) Electroless deposition of gold thin films on silicon for surface-enhanced infrared spectroelectrochemistry. *Electrochem. Commun.*, *4*, 973-977.
2. Surendranath, Y.; Kanan, M. W.; Nocera, D. G. (2010) Mechanistic Studies of the Oxygen Evolution Reaction by a Cobalt-Phosphate Catalyst at Neutral pH. *J. Am. Chem. Soc.*, *132*, 16501-16509.
3. Friebel, D.; Bajdich, M.; Yeo, B. S.; Louie, M. W.; Miller, D. J.; Sanchez Casalongue, H.; Mbuga, F.; Weng, T.-C.; Nordlund, D.; Sokaras, D.; Alonso-Mori, R.; Bell, A. T.; Nilsson, A. (2013) On the chemical state of Co oxide electrocatalysts during alkaline water splitting. *Phys. Chem. Chem. Phys.*, *15*, 17460-17467.
4. Tang, I. N.; Munkelwitz, H. R. (1994) Water activities, densities, and refractive indices of aqueous sulfates and sodium nitrate droplets of atmospheric importance. *J. Geophy. Res. : Atmos.*, *99*, 18801-18808.
5. Li, W.; Sheehan, S. W.; He, D.; He, Y.; Yao, X.; Grimm, R. L.; Brudvig, G. W.; Wang, D. (2015) Hematite-Based Solar Water Splitting in Acidic Solutions: Functionalization by Mono- and Multilayers of Iridium Oxygen-Evolution Catalysts. *Angew. Chem. Int. Ed.*, *54*, 11428-11432.
6. Frisch, M. J.; Trucks, G. W.; Schlegel, H. B.; Scuseria, G. E.; Robb, M. A.; Cheeseman, J. R.; Scalmani, G.; Barone, V.; Petersson, G. A.; Nakatsuji, H.; et al.: Gaussian 16 Rev. C.01. Wallingford, CT, 2016.
7. Becke, A. D. (1993) Density-functional thermochemistry. III. The role of exact exchange. *J. Chem. Phys.*, *98*, 5648-5652.
8. Stephens, P. J.; Devlin, F. J.; Chabalowski, C. F.; Frisch, M. J. (1994) Ab initio calculation of vibrational absorption and circular dichroism spectra using density functional force fields. *J. Phys. Chem.*, *98*, 11623-11627.
9. Weigend, F.; Ahlrichs, R. (2005) Balanced basis sets of split valence, triple zeta valence and quadruple zeta valence quality for H to Rn: Design and assessment of accuracy. *Phys. Chem. Chem. Phys.*, *7*, 3297-3305.
10. Marenich, A. V.; Cramer, C. J.; Truhlar, D. G. (2009) Universal Solvation Model Based on Solute Electron Density and on a Continuum Model of the Solvent Defined by the Bulk Dielectric Constant and Atomic Surface Tensions. *J. Phys. Chem. B*, *113*, 6378-6396.
11. Grimme, S.; Ehrlich, S.; Goerigk, L. (2011) Effect of the damping function in dispersion corrected density functional theory. *J. Comput. Chem.*, *32*, 1456-1465.
12. Kanan, M. W.; Yano, J.; Surendranath, Y.; Dincă, M.; Yachandra, V. K.; Nocera, D. G. (2010) Structure and Valency of a Cobalt−Phosphate Water Oxidation Catalyst Determined by in Situ X-ray Spectroscopy. *J. Am. Chem. Soc.*, *132*, 13692-13701.
13. Nørskov, J. K.; Rossmeisl, J.; Logadottir, A.; Lindqvist, L.; Kitchin, J. R.; Bligaard, T.; Jónsson, H. (2004) Origin of the Overpotential for Oxygen Reduction at a Fuel-Cell Cathode. *J. Physi. Chem. B*, *108*, 17886-17892.
14. Kresse, G.; Hafner, J. (1993) Ab initio molecular dynamics for liquid metals. *Phys. Rev. B*, *47*, 558-561.
15. Kresse, G.; Hafner, J. (1994) Ab initio molecular-dynamics simulation of the liquid-metal--amorphous-semiconductor transition in germanium. *Phys. Rev. B*, *49*, 14251-14269.

16. Kresse, G.; Furthmüller, J. (1996) Efficiency of ab-initio total energy calculations for metals and semiconductors using a plane-wave basis set. *Computational Materials Science*, *6*, 15-50.
17. Kresse, G.; Furthmüller, J. (1996) Efficient iterative schemes for ab initio total-energy calculations using a plane-wave basis set. *Phys. Rev. B*, *54*, 11169-11186.
18. Perdew, J. P.; Burke, K.; Ernzerhof, M. (1996) Generalized Gradient Approximation Made Simple. *Phys. Rev. Lett.*, *77*, 3865-3868.
19. Blöchl, P. E. (1994) Projector augmented-wave method. *Phys. Rev. B*, *50*, 17953-17979.
20. Kresse, G.; Joubert, D. (1999) From ultrasoft pseudopotentials to the projector augmented-wave method. *Phys. Rev. B*, *59*, 1758-1775.
21. Dudarev, S. L.; Botton, G. A.; Savrasov, S. Y.; Humphreys, C. J.; Sutton, A. P. (1998) Electron-energy-loss spectra and the structural stability of nickel oxide: An LSDA+U study. *Phys. Rev. B*, *57*, 1505-1509.
22. Jain, A.; Hautier, G.; Ong, S. P.; Moore, C. J.; Fischer, C. C.; Persson, K. A.; Ceder, G. (2011) Formation enthalpies by mixing GGA and GGA $+$ $U$ calculations. *Phys. Rev. B*, *84*, 045115.
23. Monkhorst, H. J.; Pack, J. D. (1976) Special points for Brillouin-zone integrations. *Phys. Rev. B*, *13*, 5188-5192.
24. Delaplane, R. G.; Ibers, J. A.; Ferraro, J. R.; Rush, J. J. (1969) Diffraction and Spectroscopic Studies of the Cobaltic Acid System HCoC2–DCoO2. *J. Chem. Phys*, *50*, 1920-1927.
25. Ullman, A. M.; Liu, Y.; Huynh, M.; Bediako, D. K.; Wang, H.; Anderson, B. L.; Powers, D. C.; Breen, J. J.; Abruña, H. D.; Nocera, D. G. (2014) Water Oxidation Catalysis by Co(II) Impurities in $Co(III)_4O_4$ Cubanes. *J. Am. Chem. Soc.*, *136*, 17681-17688.
26. Kwapien, K.; Piccinin, S.; Fabris, S. (2013) Energetics of Water Oxidation Catalyzed by Cobalt Oxide Nanoparticles: Assessing the Accuracy of DFT and DFT+U Approaches against Coupled Cluster Methods. *J. Phys. Chem. Lett.*, *4*, 4223-4230.
27. Bard, A. J.; Faulkner, L. R.; Leddy, J.; Zoski, C. G.: *Electrochemical methods: fundamentals and applications*; wiley New York, 1980; Vol. 2.
28. Reynolds, J. G.; Mauss, B. M.; Daniel, R. C. (2018) The relative viscosity of $NaNO_3$ and $NaNO_2$ aqueous solutions. *J. Mol. Liq.*, *264*, 110-114.